

Anisotropic mechanical and fatigue behaviour of Inconel718 produced by SLM in LCF and high-temperature conditions

Original

Anisotropic mechanical and fatigue behaviour of Inconel718 produced by SLM in LCF and high-temperature conditions / Sausto, F.; Marchese, G.; Bassini, E.; Calandri, M.; Biamino, S.; Ugues, D.; Foletti, S.; Beretta, S.. - In: FATIGUE & FRACTURE OF ENGINEERING MATERIALS & STRUCTURES. - ISSN 8756-758X. - 44:1(2021), pp. 271-292. [10.1111/ffe.13373]

Availability:

This version is available at: 11583/2873996 since: 2021-03-16T15:56:22Z

Publisher:

Blackwell Publishing Ltd

Published

DOI:10.1111/ffe.13373

Terms of use:

This article is made available under terms and conditions as specified in the corresponding bibliographic description in the repository

Publisher copyright

Wiley postprint/Author's Accepted Manuscript

This is the peer reviewed version of the above quoted article, which has been published in final form at <http://dx.doi.org/10.1111/ffe.13373>. This article may be used for non-commercial purposes in accordance with Wiley Terms and Conditions for Use of Self-Archived Versions.

(Article begins on next page)

Anisotropic mechanical and fatigue behaviour of Inconel718 produced by SLM in LCF and high temperature conditions

F. Sausto¹, G. Marchese², E. Bassini², M. Calandri², S. Biamino², D. Ugues², S. Foletti¹, S. Beretta^{1*}

¹Department of Mechanical Engineering, Politecnico di Milano, Italy, IT

²Department of Applied Science and Technology, Politecnico di Torino, Italy, IT

*Corresponding Author:

stefano.beretta@polimi.it

Submitted to:

Fatigue & Fracture of Engineering Materials & Structures

Original Submission: 26-Jun-2020

Revised Submission: 6-Oct-2020

Abstract

Additive Manufacturing (AM) is one of the processes with the most potential for producing components used in internal combustion engines, and features high efficiency due to the possibility of building very complex shapes. Several drawbacks of parts produced using AM are still unresolved, like poor surface quality, the presence of internal defects and anisotropic mechanical behaviour, that all contribute to decreasing the fatigue strength compared to the material produced using conventional processes. The effect of building direction on both the macroscopic mechanical behaviour and the crack propagation mechanism of Ni-base superalloy Inconel718 produced using AM was investigated under the combined effect of low cycle fatigue (LCF) and high temperature. The different crack growth mechanism investigated using compact tension (CT) specimens, tested at high temperature, showed a significant difference between the two building directions.

The LCF fatigue experiments also showed a significant difference in the ϵ -N curves from the two directions together with a high level of scatter, due to the dispersion of the defect size at the fracture origin. The dimensions of the defects (as measured using the \sqrt{area} parameter) were analysed by means of extreme value statistics and showed a significant difference between the two orientations investigated.

The aim of this work is to propose a simplified approach (based on ΔJ_{eff} concepts) to estimate the fatigue life of a component produced using AM that takes into account the material variability due to the combined effect of mechanical anisotropic behaviour and the presence of defects at high temperature conditions.

Keywords: Additive Manufacturing; Inconel718; High temperature; Selective Laser Melting; Nickel based superalloy; Low Cycle Fatigue.

Nomenclature

a	crack depth	R_σ	stress ratio
c	surface crack length	Y	crack shape factor
C, m	coefficients of the Paris law	α	constraint factor
da/dN	crack propagation rate	$\Delta\varepsilon$	strain range
E	stabilized Young's modulus	$\Delta\sigma$	stress range
E'	Young's modulus for plane strain condition	ΔJ	cyclic J-integral range
K', n'	Ramberg-Osgood parameters	σ_a	alternate stress
N_f	number of cycles to failure	$\sigma_f', \varepsilon_f', b, c$	Coffin-Manson curve parameters
PJ	crack length independent damage parameter	ε_a	alternate strain
R_ε	strain ratio	λ, δ	LEVD parameters
R_m	tensile strength	ν	Poisson's ratio
$R_{p,0.2}$	0.2% proof strength		

Acronyms

AM	additive manufacturing	LEMF	linear elastic fracture mechanics
CT	compact tension (specimen)	LEVD	largest extreme value distribution
FCG	Fatigue crack growth	LoF	lack of fusion
FEM	finite element modelling	LOM	light optical microscope
FE-SEM	field emission scanning electron microscope	SEM	scanning electron microscope
EDM	electric discharge machining	SIF	stress intensity factor
EPFM	elasto-plastic fracture mechanics	SLM	selective laser melting
LCF	low cycle fatigue	EIFS	equivalent initial flaw size

1. Introduction

Inconel718 is a Nickel-based superalloy widely used in aeronautic sectors due to its excellent mechanical and fatigue properties also at high temperatures, enabling its use under load up to around 650-700 °C. Additionally, the alloy offers very high corrosion and oxidation resistance ^{[1], [2]}.

This alloy has been widely processed using AM techniques such as selective laser melting (SLM) and direct laser deposition. More specifically, selective laser melting is a powder bed fusion process in which a laser beam selectively melts a layer of loose powder. These advantages make it possible to produce very complex mechanical components, that simultaneously satisfy energy efficiency (due to the optimized obtained shape) and ease of assembly due to a reduced number of parts ^{[3], [4]}, overcoming the issues of traditional manufacturing techniques such as high mechanical properties and hardness; making them challenging to be machined ^{[5], [6]}.

Several studies have paid attention to the microstructure and mechanical properties of Inconel718 processed by SLM ^{[1], [7]–[16]}. Due to its high weldability, the SLM process guarantees the production of components with a very low quantity of defects ^{[13], [17], [18]}. However, the as-built microstructure derived from very high cooling rates (10^5 - 10^6 °C/s) ^{[2], [13], [19]} leads to a very fine microstructure made up of fine dendritic/cellular structures with possible micro-segregations and Laves phases. Moreover, the heat flux results in forming columnar grains along the building direction, creating an anisotropic microstructure ^{[1], [2], [13], [20]}.

It is well known that the orientation of the loading direction in relation to that of printing influences the fatigue life of material obtained by means of AM. The effect of building orientation on fatigue strength of 17-4 PH stainless steel, produced using SLM, in LCF conditions was investigated in ^[21] at room temperature. For this alloy it was demonstrated that the cyclic response of the material differs from one orientation to the other. The specimens printed in a vertical direction show a lower cyclic yielding stress compared to the horizontal ones. Another parameter influenced by the material orientation in relation to the loading direction, is the dangerousness of the manufacturing defects. AM process produces two main types of internal defects, a lack of fusions (LoFs) and pores. Of these two types the LoFs are more detrimental than the pores, due to its irregular shape. Moreover, these kind of defects are elongated perpendicular to the building orientation, hence the LoFs reduce the fatigue strength of vertical oriented more than horizontal oriented material. These factors lead to a longer fatigue life for the horizontal than for the vertical specimens with the material in “machining” condition.

Shrestha et al. in [22] investigated both the effect of the building orientation and the surface roughness on the strain life of 316L stainless steel, at room temperature, manufactured using laser beam powder bed fusion (LB-PBF). Also for this alloy the orientation of the loading direction in relation to the building plan influences the mechanical behaviour of the material, showing a lower cyclic yield stress for the specimens printed in a vertical direction than those printed horizontally. In turn this effect influences the strain life of the specimens. Despite the lower cyclic properties of the vertical oriented specimens, their fatigue life was lower than that for the horizontal ones; this was due to the different detrimental effect of the orientation of the defects inside the material, making them more prone to crack initiation in vertical oriented specimens.

The impact of building orientation on fatigue crack growth was investigated for 316L stainless steel at room temperature produced using SLM in the work by Riemer et al. [23]. The main conclusion of this work was that a crack propagates faster in the horizontal oriented specimens than the vertical ones. This evidence was explained considering the orientation of the material grains, which are elongated parallel to the building direction; when a crack propagates in vertical oriented material, it slows down due to grain boundaries that act as a barrier. On the other hand, in the horizontal specimens the crack propagates parallel to the building direction passing through fewer grain boundaries and hence propagating faster.

In a recent work by Lindstorm et al. [24] the anisotropic mechanical behaviour of the Ni-based superalloy Hastelloy X was investigated in LCF conditions at room temperature. The mechanical response of the material varies between the specimens printed at 0° in relation to the building plane and the 90° oriented ones. To take into account the high level of anisotropy, a bi-linear elasto-plastic model was set-up. The fatigue life depends on the printing orientation. To take into account this effect a multiaxial criterion based on the Smith-Watson-Topper (SWT) model was fitted on the experimental results and showed a good correlation. No defects effect were considered in the fatigue life model.

Due to the prospective advantages of Inconel718 produced via AM, the scientific research into the mechanical and fatigue performance of this super-alloy has growing in recent years. The influence of internal defects and rough as-built surfaces on the high cycle fatigue (HCF) regime was investigated in [25]–[27], while the effect of microstructure on the low cycle fatigue (LCF) was investigated in [28], [29]. What emerges from these works is that for a reliable fatigue analysis one cannot ignore the combined effect of manufacturing defects (internal and superficial) and the anisotropic mechanical behaviour due to the microstructure obtained. For this reason a pseudo-elastic stress amplitude approach was adopted in [30] to model the LCF strength of this alloy for different

building orientations and heat treatments. However, Ni-based superalloys produced with conventional manufacturing processes, are primarily used in high temperature environments due to their elevated heat resistance properties. There is therefore a stringent requirement of scientific investigation of fatigue properties of these alloys produced using AM, operating under high temperature conditions. The effect of an elevated environmental temperature on fatigue strength of Inconel718 was investigated in [31], [32].

The impact of different layer orientations on the fatigue strength of Inconel718 AM at 650 °C, was investigated in [31]. The conclusion of this work was that the material with the columnar grains oriented parallel to the main loading direction showed a longer fatigue life than the other orientations. Moreover, it was demonstrated that the overall fatigue life of Inconel718 produced using AM was comparable to its wrought material counterpart.

The fatigue properties of Inconel718 produced using laser beam directed energy deposition (LB-DED) under high temperature conditions, was investigated in a recent work by Nezhadfar et al. [32]. In this paper it was found that the fatigue resistance of AM Inconel718 at high temperature was lower than that at room temperature. This was found to be due the formation of more δ and Laves phases during fatigue testing at high temperature; because these phases are brittle they break under high strain conditions accelerating crack advancement. Also in this work what emerges was that the fatigue resistance of AM material is comparable with material manufactured using conventional process at a temperature of 650 °C.

The aim of this paper is to deal with a different kind of approach, where the fatigue life of Inconel718 produced by SLM is estimated using a crack growth algorithm and the statistical population of the manufacturing defects. This kind of approach was already adopted for LCF life prediction of AlSi10Mg manufacturing using SLM in [33]. This approach makes it possible to directly estimate the effects of both intrinsic material anisotropy and the different defect populations between one printing orientation and the other.

This paper is subdivided as follows. In **Section 2** an overview of the material microstructure and manufacturing process as well as the experimental methodologies adopted are explained. In **Section 3** the main results from the LCF and long crack propagation tests are shown and discussed. **Section 4** is dedicated to the explanation and validation of the proposed model for assessing the life prediction of material produced using AM, taking into account the effect of different manufacturing orientations. The paper closes with a discussion on the main conclusions of this work in **Section 5**.

2. Material and experiments

Specimens tested in this work were machined from rod bars and parallelepipeds obtained using additive manufacturing (AM); the dimensions of the cylinders for LCF tests prior to machining were 125 mm in height and 16 mm in diameter, while the parallelepipeds for the CT specimens were 35x34x17 mm³. An EOSINT M270 Dual Mode machine equipped with a 200W Yb fibre laser with a 100 µm spot was used.

The process parameters consisted of laser power of 195 W, scanning speed of 1200 mm/s, hatching distance of 0.09 mm, and layer thickness of 20 µm using the scanning strategy involving rotation of 67° between different layers. This is the standard strategy of laser rotation suggested by EOS to reduce the anisotropy along the x-y plane. Moreover, the process occurs with a preheating temperature of the building platform to 80 °C. The operating process parameters make it possible to limit the defects within the samples, thus improving the densification of the alloy [12], [13]. The gas atomized Inconel718 powder was purchased from EOS GmbH with a particle size distribution of d10 ≈ 19 µm, d50 ≈ 26 µm and d90 ≈ 39 µm, as reported in the previous study [13].

The powder exhibits spherical particles, but also satellites and irregular particles can be detected, as highlighted in **Fig. 1**.

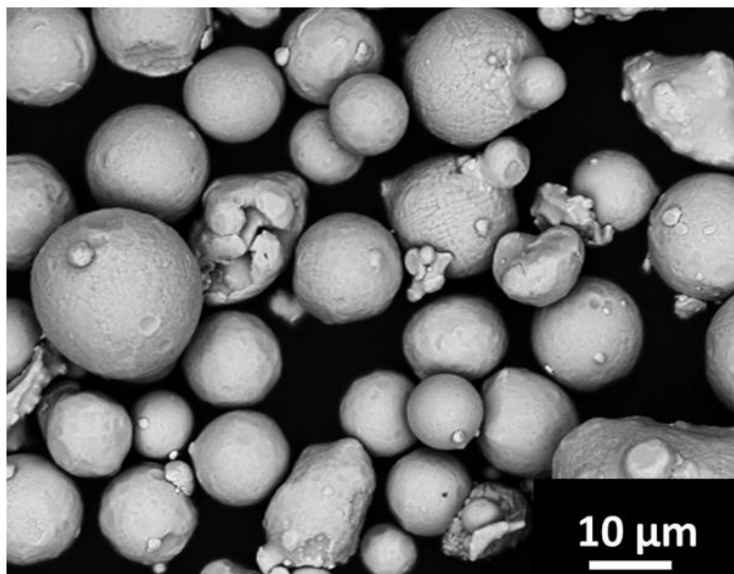


Figure 1: SEM image of the particles of Inconel718 alloy.

The declared chemical composition of the powder in wt% is provided in **Table 1**.

Ni	Cr	Nb	Mo	Ti	Al	Fe	Co	Cu	C	Si+Mn	P+S	B
50-55	17-21	4.75-5.5	2.8-3.3	0.65-1.15	0.2-0.8	Bal	<1	<0.3	<0.08	<0.35	<0.015	<0.06

Table 1: Chemical composition of metallic powder used to 3D print the specimens provided by EOS GmbH.

To study the anisotropic behaviour of Inconel718 at high temperature, both the LCF life of the material and the long crack propagation were studied. The printed bars and parallelepipeds were machined to obtain LCF and compact tension (CT) specimens respectively. A total of 8 specimens for each printing directions were obtained for the LCF tests; 2 CTs specimens for each series were obtained for the crack propagation tests, with an additional one printed in XY direction used for thermal calibration. The specimens were printed in a vertical and horizontal direction in relation to the printing plane; from now on the vertical and horizontal specimens will be referred to as *Z-series* and *XY-series* respectively. A schematic representation of the specimens' printing directions and their main dimensions, is reported in **Fig. 2**.

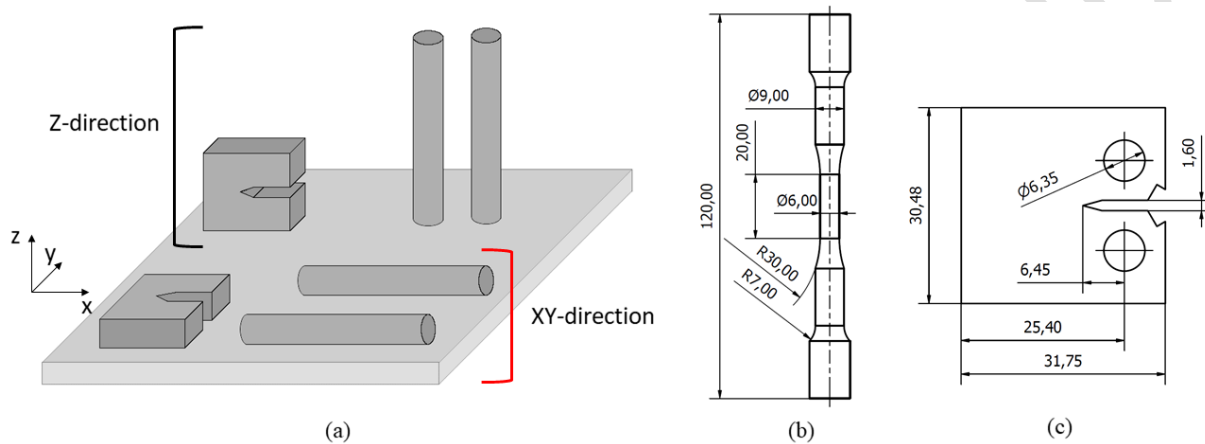


Figure 2: Manufacturing of the specimens and their geometry: a) printing directions of the rough geometry of the specimens; b) uniaxial specimen for low cycle fatigue (LCF) tests at high temperature according to ASTM E606 [34], all the dimensions are in mm; c) compact tension (CT) specimen for fatigue crack growth at high temperature according to ASTM E647 [35], all the dimensions are in mm.

Before machining the material was subjected to a thermal treatment, which consisted of solution annealing at 1065 °C for 2 hours followed by double ageing at 720 °C for 8 hours and then 630 °C for 8 hours. The first solution annealing treatment homogenizes the microstructure, preparing the alloy for the formation of the strengthening γ' and γ'' phases thanks to the subsequent ageing treatments [1], [19]. The annealing solution recipe was designed in a previous work by some of the authors [12]. These annealing parameters make a high level of dissolution of precipitates possible, as well as homogenizing the chemical composition of the alloy. This aspect is crucial to promote a uniform dispersion of precipitates during the aging treatments.

The grain shapes and texture of the heat-treated material was characterized using an FIB-SEM equipped with an electron backscatter diffraction (EBSD) detector. The specimens were tilted by 70° and scanned at 20 kV, with around 4 μm step, investigating the samples along the Z and XY orientations. Figure 3 shows the EBSD maps of the material in the Z and in the XY directions in the as-heat treated state. In the Z direction (**Fig. 3.a**), grains appear elongated and preferentially oriented

parallel to the building direction. This typical microstructure is inherited from the As-Built state due to the particular manufacturing process which takes place during AM. These features are not eliminated by the subsequent heat treatment as described in a previous work by Calandri et al. [12] that also pointed out that only an annealing temperature as high as 1200 °C may eliminate this elongated grains structure. The XY plane (**Fig. 3.b**), on the other hand, presents a more equiaxed microstructure, characterized by roundish grains. Finally, a strong texture along the {001} orientation can be observed.

Because of the heat treatment described previously, several precipitates were formed (see **Fig. 4**). According to a former work by Calandri [13], the particles observed at the grain boundaries can be referred to as carbides and in **Fig. 4** they are highlighted by green arrows, while inside the grains, the homogeneous precipitation of a mixture of nanometric γ' and γ'' precipitates is shown in the green box at high magnification. A difference must be pointed out between XY and Z sections as regards the distribution of carbides: within an equiaxed microstructure, typical of the XY sections, the carbides precipitation is much more even and homogeneously distributed, thus carbide networks are less visible while within the columnar microstructure, typical of the Z sections, these particles form more evident networks.

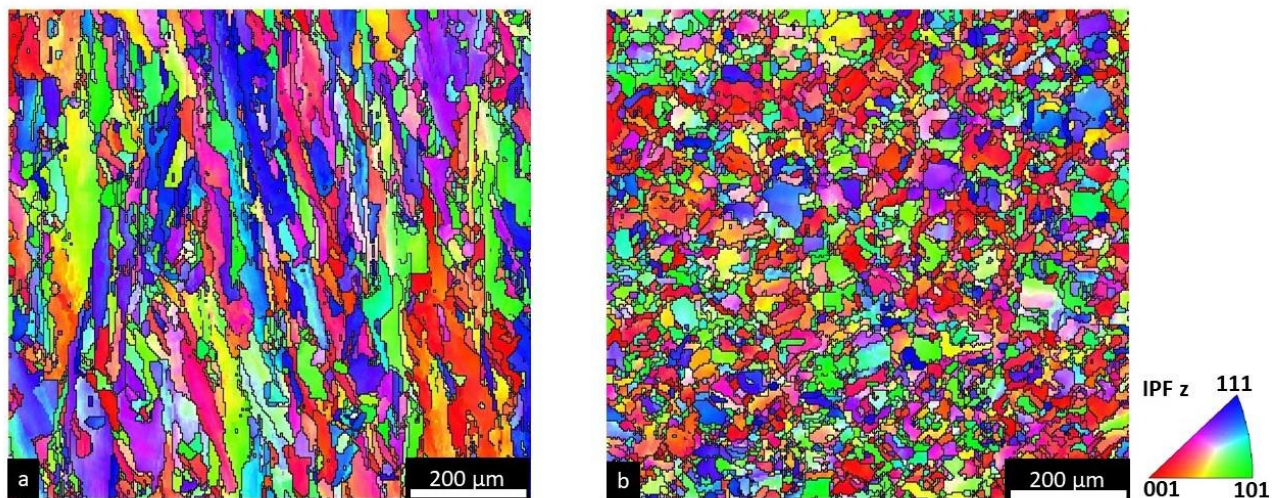


Figure 3: (a,b) Electron backscattered diffraction (EBSD) maps with inverse pole figure (IPF) with high angle grain boundaries ($> 10^\circ$) marked in black lines. Samples were observed along the Z (a) and XY (b) plane.

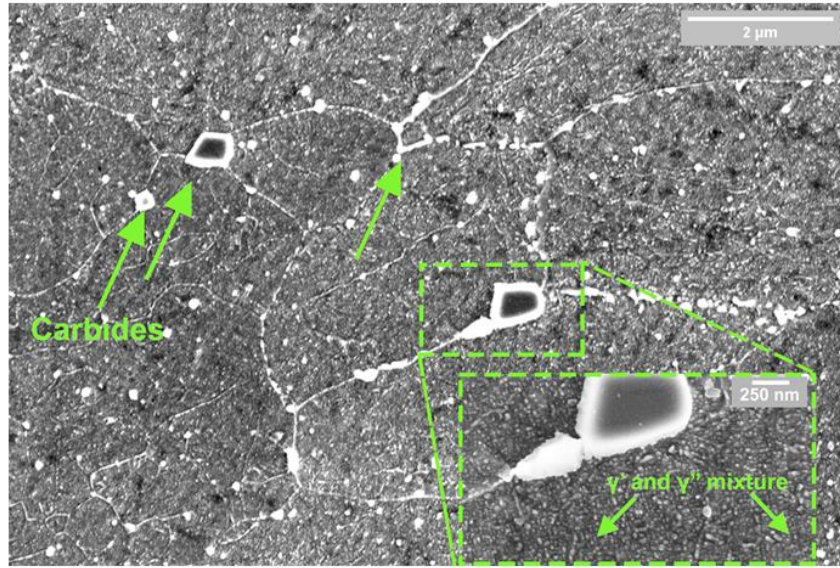


Figure 4: XY sample observed at high magnification to better describe the reinforcing particles and the intergranular carbides.

Accepted Manuscript

2.1 Low cycle fatigue tests

The specimens used to characterize the fatigue life of the alloy considered, were manufactured in accordance with the specifications of the ASTM E606 [34] standard. The main dimensions of the specimens considered are reported in **Fig. 2.b**. The fatigue tests were conducted under strain control logic, on a servo-hydraulic MTS Landmark testing machine able to apply a maximum force of 100 kN equipped with a resistance furnace Hot Box AST 3160 with a maximum temperature of 1000 °C. The strain evolution during the cyclic fatigue was monitored using an MTS extensometer, model 623.54F-14, with a base measuring length of 12 mm, equipped with ceramic rods the end of which are specifically shaped for cylindrical tensile specimens.

To guarantee a uniform temperature distribution along the specimens, preliminary thermal calibration was required. A dummy specimen, with the same geometrical and material characteristics as those tested, was equipped with K-type thermocouples, which were spot welded onto the parallel length gauge. One thermocouple was welded at the mid-position of the specimen, while another two were welded on both the upper and lower side of the gauge section at a distance from the mid specimen's plane of 6 mm and 10 mm respectively. A total of 5 thermocouples were spot welded onto the specimen. The signal from the thermocouples was acquired with an external reader, while the temperature of the furnace was monitored via two integrated thermocouples which controlled the power of the two active resistances. The two furnace resistances were set in order to have each thermocouple at a temperature equal to:

$$T_i = T_n \pm \Delta T \quad (1)$$

where T_i is the i -th thermocouple temperature, T_n is the target temperature and ΔT is the maximum value between 2 °C or 1% of T_i as required by the ASTM E606 [34] standard. Once the temperature of the furnace reached the target, a minimum delay of 30 min was considered for allowing temperature stabilization before starting the test. The tests for both Z and XY series were performed at a frequency of 0.5 Hz, with an imposed strain ratio of $R_\epsilon = 0$. A total of 8 specimens were tested printed in Z orientation, while 7 specimens were tested printed in XY orientation. One of the available XY specimens available was used for the thermal calibration, and hence discarded from testing.

2.2 Fracture analysis

At the end of each fatigue test, the specimen was cooled down in liquid nitrogen and statically broken to obtain a fragile rupture of the material surrounding the fatigue crack. Before performing the fracture analysis, the specimens' surfaces were sonicated in ethanol to eliminate any dirt or dust. In case of a very dirty surface, thorough manual polishing was performed using ethanol and the mechanical action of a toothbrush. The fracture surfaces obtained were initially observed using a

stereomicroscope to have a global inspection of the cracks, then a more accurate analysis using the scanning electron microscope (SEM) was performed. The analysis of the killer defects was carried out using the SEM EVO 50 by Zeiss. A further analysis of the damaged surface featured by fatigue striations, was performed with the field emission SEM (FE-SEM) Sigma 500 manufactured by Zeiss.

2.3 Fatigue crack propagation tests

The printed parallelepipeds, were milled in order to reach the dimensions shown in **Fig. 2.b** and a thickness of 12.6 mm in accordance with ASTM E647 [35]. The sharp notch and the extensometer housing, were obtained using wire EDM. After machining, the CT specimens were polished using emery paper with a grain of 320 to 2500 in order to reach a semi-mirrored quality of the surfaces perpendicular to the starter notch. The CT specimens were pre-cracked in tension at room temperature on a servo-hydraulic MTS Landmark testing machine, using the ΔK -decreasing technique; a frequency of 20 Hz was imposed. The procedure was continued until an initial crack length of 7.7 mm was reached. As for the LCF tests, for the crack propagation test a dummy specimen was equipped with K-type thermocouples to set the optimal furnace temperature. Three thermocouples were spot welded on both the specimen's surfaces at 4 mm from the starter notch: one on the mid-plane, and the other two placed 3 mm from it on both upper and lower side. Tests were carried out using the same test rig as for the LCF tests. The crack length evolution was calculated with the procedure specified in ASTM E647 [35] from the compliance curve, which is acquired during the test from the testing machine's load cell and the signal of a clip gauge Epsilon COD HIGH TEMP 3548-COD-005M-040M-ST with a base measuring length of 5 mm equipped with ceramic rods. A frequency of 15 Hz was considered in the current tests, which was proven to not affect the results at high temperature for the same wrought alloy [36]. At the end of each test, the specimens were statically broken after cooling in liquid nitrogen to obtain a fragile rupture of the remaining ligament. The fracture surfaces were observed under an optical microscope to obtain the real initial and final crack length, which were used to correct the measurements obtained during the test as in accordance with ASTM E647 [35] and ASTM E399 [37]. A total of 2 specimens for each series was tested at two stress ratios $R_\sigma = 0.05$ and $R_\sigma = 0.70$.

3. Results

3.1 Mechanical behaviour of material

The alternate strain versus stress of the stabilized hysteresis loops of the LCF tests, are plotted in **Fig. 5.a**. The experimental results of the strain fatigue tests performed at 1000 °F (538 °C) and strain ratio $R_\epsilon = 0$, are shown in **Fig. 5.b** and are reported in **Table 10** and **Table 11** in the Appendix in terms of the stabilized stress-strain cycles at 50% of life for Z and XY series respectively. The fatigue data for the wrought material is taken from literature, while the data at 550 °C was reported in the work by Fournier [38] and that at 650 °C was reported in the work by Brinkman [39]. The experimental amplitude of the stress versus strain data set, was fitted with a Ramberg-Osgood curve:

$$\epsilon_a = \frac{\sigma_a}{E} + \left(\frac{\sigma_a}{K'}\right)^{\frac{1}{n'}} \quad (2)$$

where E is the stabilized Young's modulus, σ_a is the alternate stress and K' and n' are the hardening coefficient and exponent of the plastic part of the stabilized cyclic curve respectively. The fitted coefficients are reported in **Table 2**.

Looking at the experimental results the anisotropy induced by the printing process is evident. In particular, from the analysis of the two cyclic curves plotted in solid lines in **Fig. 5.a**, a lower cyclic yield stress can be noted for the specimens printed in the Z direction. The printing process imposes a thermal gradient that is parallel to the building direction; this forces the grains to grow parallel to the gradient. The microstructure obtained results in elongated grains parallel to the laser beam, in particular the crystallographic direction {001} is shown to be perpendicular to the building platform. Ni et al. [20] explain the lower yielding stress at room temperature of tensile specimens of Inconel718 printed in a vertical direction than to the horizontal ones, by considering the Schmid factor for the two series. The Schmid factor of the material printed in the vertical direction is higher than the one printed horizontally, this indicates that the dislocations in the Z direction are more prone to sliding than those in the XY direction. This observation is still valid in the case of LCF conditions at high temperatures as well, and can be used to explain the differences between the cyclic curves for the Z and XY series.

Considering the cyclic curves obtained in **Fig. 5.a**, a certain imposed alternate strain corresponds to a stress that is higher for the XY series than to the Z ones. This directly affects the fatigue life, that is lower for the XY series than for the Z ones at the same strain level as shown in **Fig. 5.b**.

The fatigue lives obtained were fitted with an endurance curve of the Coffin-Manson type [40]:

$$\varepsilon_a = \varepsilon_{a,el} + \varepsilon_{a,pl} = \frac{\sigma_f'}{E}(2N_f)^b + \varepsilon_f'(2N_f)^c \quad (3)$$

where ε_a is the total strain amplitude, $\varepsilon_{a,el}$ and $\varepsilon_{a,pl}$ are the elastic and the plastic alternate strains, σ_f' and ε_f' are the fatigue strength and the ductility coefficients, b and c are the fatigue strength and ductility exponents and N_f is the number of cycles to failure. Due to the very low level of plastic strain reached during the experiments, only the elastic part of the Coffin-Manson curve was used to fit the results. The solid markers in **Fig. 5.b** for the tested specimens printed in the Z direction were included in the fitting of the Coffin-Manson curve, while the empty blue dot was excluded. This point was excluded because the main crack originated from an internal defect unlike the others that originated from superficial ones, as it is discussed in **Section 3.2**. The curves obtained were plotted in dashed lines with the experimental points in **Fig. 5.b** while the fitting coefficients are reported in **Table 3**.

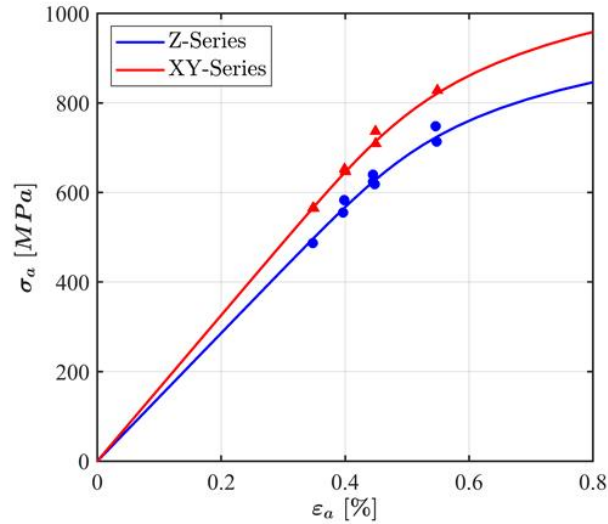
The experimental data points for the two printing directions, were then compared with the fatigue data of the wrought Inconel718 tested at similar temperatures in **Fig. 5.b**. As can be seen the fatigue performance of the AM material at high temperature are not very far from its wrought counterpart, that are good for the Z direction and worse for the XY direction.

Printing direction	E_{stab} [MPa]	n'	K' [MPa]
Z	142952	0.0964	1534.42
XY	162901	0.0993	1766.51

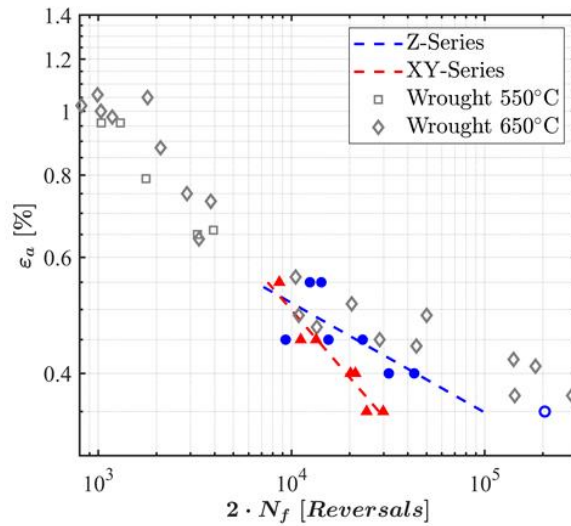
Table 2: Fitting coefficients of the stabilized Ramberg-Osgood cyclic curve.

Printing direction	σ_f' [MPa]	b
Z	3388.35	-0.1664
XY	18749.50	-0.3407

Table 3: Fitting coefficients of the elastic part of the Coffin-Manson curves for describing the experimental results for the two printing directions.



(a)



(b)

Figure 5: LCF results obtained at 1000 °F: a) alternate strain versus stress of the stabilized mid-life hysteresis loop; b) strain versus life for the tested specimens printed in vertical and horizontal directions in relation to the building plate (Z and XY series respectively). Wrought data is taken from the works by Fournier [38] and Brinkman [39].

3.2 Analysis of the fracture surfaces

The results of the fracture surfaces are reported for two specimens printed in the Z and XY directions in **Fig. 6** and **Fig. 7**, coded as Z8 and XY7 respectively. Specimen coded XY3 failed due to a crack that originated out of the gauge section, for this reason it was excluded from the analysis.

For both series the main crack originates from manufacturing defects, as shown in detail in **Fig. 6.b** and **Fig. 7.b**. Both the defects found featured an irregular shape which is characteristic of LoF; no pores were found to have generated fatigue cracks. The defect dimensions were described in terms of square root of the area projected onto the crack plane, the results obtained are reported in

Table 4. Manufacturing defects can be classified as internal and superficial. A simple empirical rule that can be used to categorize defects was proposed by Murakami [41], that, supposing a circular shaped defects, has the following formulation:

$$\frac{r}{h} > 0.8 \quad (4)$$

where r is the radius of the equivalent circle and h is the length from the free specimen surface to the centre of the defect. According to this rule, all the defects found were categorized as superficial except for specimen Z5 that featured an internal defect.

The work of Fournier et al. [38] showed that wrought Inconel718 fails due to the formation of shear bands by twinning, from which cracks nucleate and grow. This mechanism is accentuated at high temperature [38]. In wrought material the formation of shear bands is mainly associated with the orientation of the grains in relation to the main loading axis, which rules the activation of one of the 12 slip planes of the FCC lattice. A defect inside the material can be classified as a stress riser, that interacts with the microstructure if its dimension is similar to that of the material's grains [42]–[45], resulting in the activation of one or more slip systems. A crack that originates from the activation of a slip plane, is characterized by a flat, smooth surface in the initiation region. The defects responsible for the final failure of the specimens featured a flat surface surrounding them, indicating the slip of a material plane in the first phase of crack propagation.

For both the printing directions the crack propagation featured smooth facets, onto which striations lines can be clearly identified as shown in **Fig. 6.c-e** and **Fig. 7.c-e**. The presence of these features indicates that the crack propagation is mainly transgranular, as reported in a recent work by Nezhadfar et al.[32]. In 1960 Forsyth [46] demonstrated that the spacing between striation lines calculated at different crack lengths, correlates well with the macroscopic crack propagation curve. This methodology was later applied in [47] and [48], showing a good correlation between the macroscopic crack propagation curve and the crack speed computed from striation spacing for different materials. Following the suggestion by Forsyth [46], in this work several locations on the crack surfaces were examined at high resolution to pinpoint striations. The mean crack propagation speed was estimated considering a set of N_S striation lines characterized by a length d , as the ratio between d and N_S . For each estimation of the crack speed, the crack length was considered as the radius of the semicircle centred in the initiation region passing through the mid-point of the captured figure; this is schematically shown in **Fig. 6.a** and **7.a**. As shown in **Fig. 6.d-f** and in **Fig. 7.d-f**, the crack growth rate computed from striation analysis increases as the crack front approaches final rupture. The obtained results are reported in **Table 5** and **Table 6** for the Z and XY series of specimens respectively.

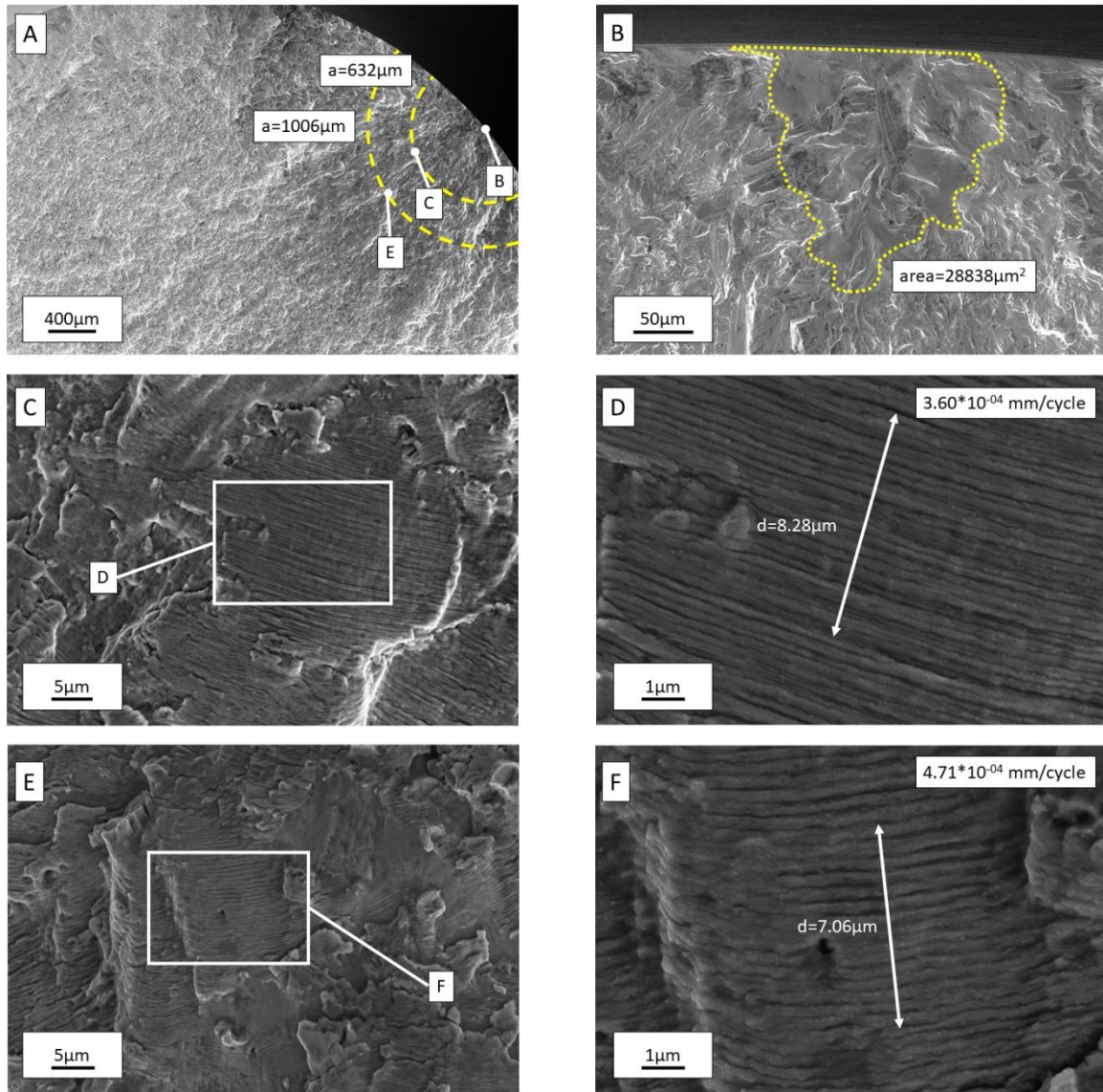


Figure 6: Main features of the fracture surface of specimen Z8: a) global picture of the main crack; b) detail of the killer defect, its boundaries are highlighted with a yellow dashed curve; c) and d) details of the striations lines found that correspond to a crack length of 623 μm and $3.6 \cdot 10^{-4}$ mm/cycle propagation velocity; e) and f) details of the striations lines found that correspond to a crack length of 1006 μm and $4.7 \cdot 10^{-4}$ mm/cycle propagation velocity.

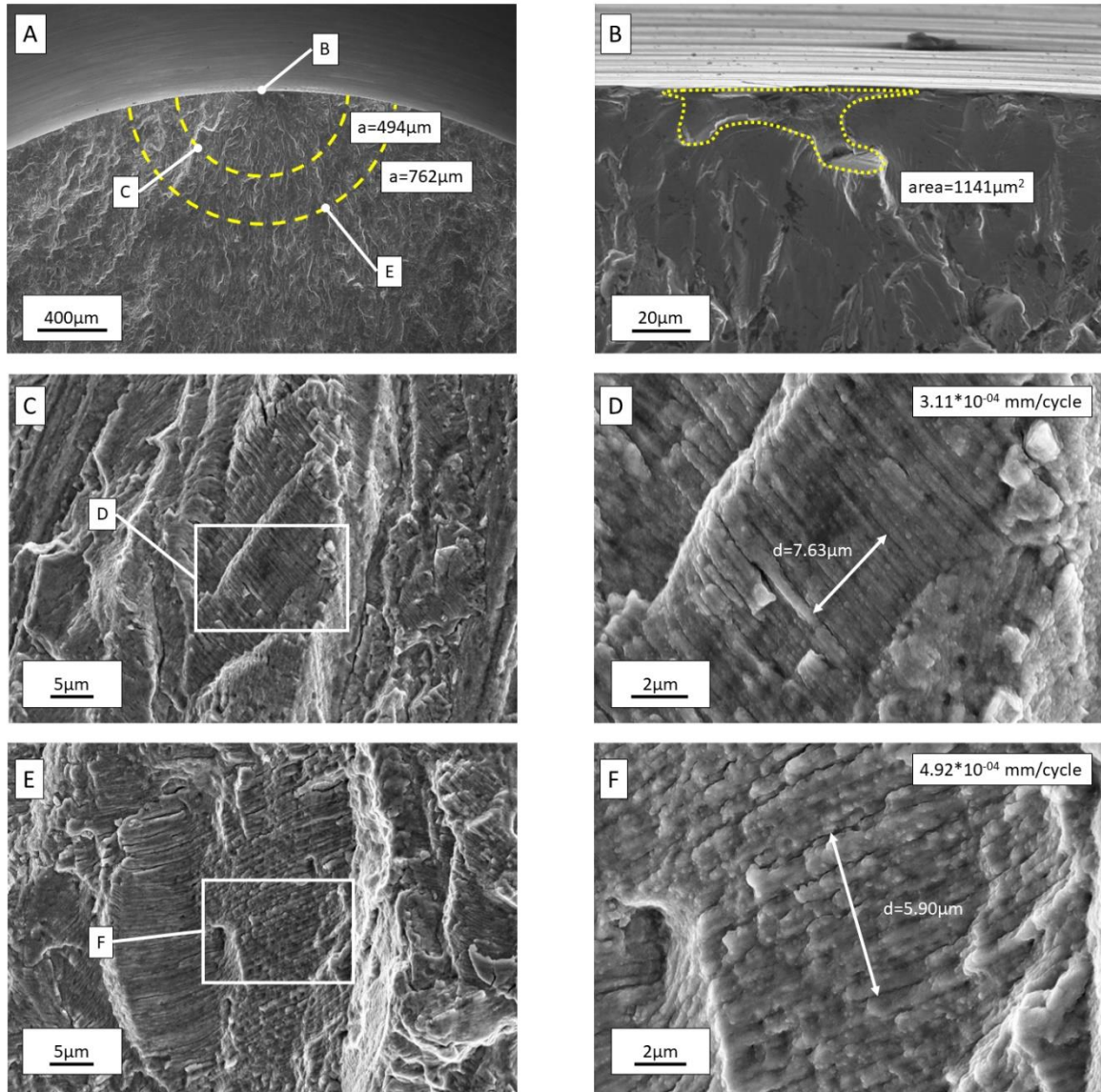


Figure 7: Main features of the fracture surface of specimen XY7: a) global picture of the main crack; b) detail of the killer defect, its boundaries are highlighted with a yellow dashed curve; c) and d) details of the striations lines found that correspond to a crack length of 494 μm and $3.11 \cdot 10^{-4}$ mm/cycle propagation velocity; e) and f) details of the striations lines found that correspond to a crack length of 762 μm and $4.92 \cdot 10^{-4}$ mm/cycle propagation velocity.

ID	\sqrt{area} [mm]	ID	\sqrt{area} [mm]
Z1	0.0725	XY1	0.0395
Z2	0.1339	XY4	0.0297
Z3	0.1217	XY5	0.0239
Z4	0.1065	XY6	0.0350
Z5	0.0648	XY7	0.0338
Z6	0.1768	XY8	0.0345
Z7	0.0462		
Z8	0.1698		

Table 4: Dimensions of the manufacturing defects responsible to the final rupture of specimens belonging to the Z and XY series.

Z3		Z5		Z7		Z8	
da/dN [mm/cycle]	a [mm]						
2.46E-04	0.568	4.29E-04	0.605	1.62E-04	0.271	3.60E-04	0.632
3.56E-04	0.800	5.22E-04	1.103	4.73E-04	0.618	4.71E-04	1.006
9.63E-04	0.984	7.46E-04	1.717	1.23E-03	1.483		

Table 5: Results of the estimated crack speed at different advancements for LCF specimens printed in the Z direction.

XY4		XY5		XY7		XY8	
da/dN [mm/cycle]	a [mm]						
7.63E-04	0.625	9.41E-04	0.686	3.11E-04	0.494	8.29E-04	0.430
1.08E-03	0.865	1.09E-03	0.859	4.92E-04	0.762	1.56E-03	0.990
*	*	*	*	*	*	2.62E-03	1.755

Table 6: Results of the estimated crack speed at different advancements for LCF specimens printed in the XY direction.

3.3 Defect distribution and statistics of extremes

In the previous sections, we showed that the final crack responsible for the failure of a specimen always originates from a defect. This can be classified as the "killer defect", being the largest one inside the most stressed material volume [41]. The defect sizes obtained from the fracture surfaces observations, therefore represent the maximum specimens gauge section. These can be described, according to the theory of statistics of extremes, with a largest extreme values distribution (LEVD), the cumulative density function of which has the expression reported in **Equation 5**:

$$F_{LEVD} = \exp \left[- \exp \left(- \frac{x - \lambda}{\delta} \right) \right] \quad (5)$$

The probability chart of the fitted distributions with a confidence band at 95% is compared with the experimental data point in **Fig. 8**, while the values of the parameters are reported in **Table 7**. The grey shaded band in **Fig. 8** represents the lower bound for defects that could lead to a significant effect on the fatigue life of Inconel718 [44], [45].

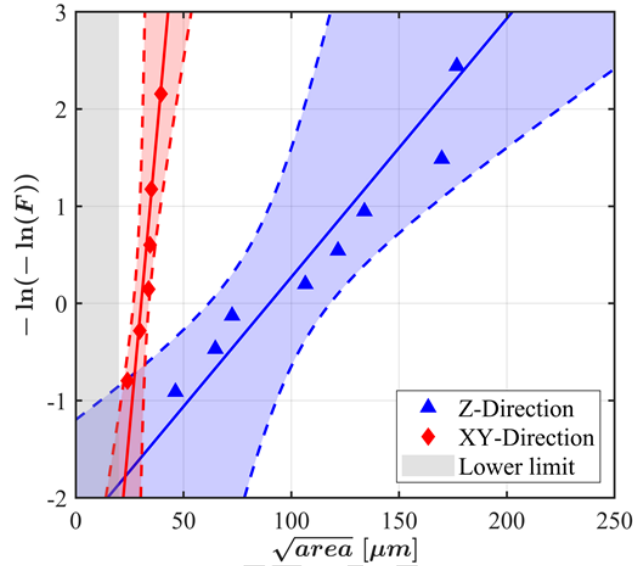


Figure 8: Probability charts for the two fitted distributions of killer defects for the two printing directions. The dashed areas correspond to 95% confidence bands for the estimated distributions.

Printing directions	λ [mm]	δ [mm]
Z	0.090	0.038
XY	0.030	0.004

Table 7: Parameters of the LEVD distribution of defects found for the two printing directions.

As can be seen, the killer defect sizes of the specimens printed in the XY direction are smaller than those printed in Z direction. This result is in agreement with other works on different materials obtained using AM, like 17-4 PH stainless steel [21] and 316L stainless steel [22].

However, the different defect sizes for the two printing directions seem to contradict the results of the LCF tests because series Z have a life longer than the one of XY specimens. This is due to the elasto-plastic driving force ahead of the defects and it will be discussed in **Section 4**.

3.4 Crack propagation tests on CT specimens

To characterize fatigue crack propagation in Inconel718, two series of CT specimens were tested. The tests were performed at two stress ratios $R_\sigma = 0.05$ and $R_\sigma = 0.70$ for both the printing directions. The results were then fitted with a Paris' law:

$$\frac{da}{dN} = C \cdot (\Delta K)^m \quad (6)$$

where C and m are the parameters of a straight line which interpolates the results in a loglog scale plot. The slope of the Paris' law m was fitted for both the printing directions considering the data with the stress ratio $R_\sigma = 0.05$, and was considered constant for the stress ratio $R_\sigma = 0.70$. The results of the fitting are shown in **Fig. 9.a** and **Fig. 9.b** for the Z and XY direction respectively, and are reported in **Table 8**.

The grey bands in **Fig. 9** corresponds to literature data taken from the work by James [49], fitted with a linear law in loglog coordinates with a scatter band of 95%. As can be seen, the results for the Z series at stress ratio $R_\sigma = 0.05$ shown a lower crack speed then the wrought material at the same level of ΔK ; meanwhile the results for the XY direction are very similar.

As can be appreciated in **Fig. 9**, the crack propagation velocity is higher for the XY than for the Z material. The different crack propagation rate in the Z and XY directions observed macroscopically in CT samples may be related to a different propagation behaviour, which, in turns, can be linked to the material's anisotropy. Regarding this latter topic, it is well known that Inconel718 presents strong anisotropy with columnar grains growing along the building direction due to the heat flux dissipation during production. Due to the texture, the samples built along the XY plane are characterized by higher tensile strengths (yield strength and ultimate tensile stress) and lower ductility than samples fabricated along the building direction (Z axis). Even the application of a subsequent solution annealing treatment at high temperature (around 1080-1100 °C) followed by a double ageing treatment is not effective in eliminating the original structures of the columnar grains, and consequently, the samples still exhibit anisotropic mechanical properties [12], [13]. For instance, Chlebus et al. [1] revealed that after solution annealing at high temperature (1100 °C for 1 hour) followed by double ageing treatment, the heat treated samples present higher tensile properties when built along the XY plane. Moreover, it was pointed out that the anisotropic microstructure also influences the crack propagation within the material. In more detail, Ni et al. [20] reported that the reduced ductility for samples built along XY plane derived from the accelerated crack formation due to the orientation of the applied tension in relation to the columnar grains. This is in accordance with the current results where the crack propagation rate is always higher in the XY samples.

This experimental data can be reinforced and discussed observing the different propagation behaviour, from a microstructural point of view, in the Z and XY oriented specimens. Z and XY samples, tested at $R_\sigma = 0.05$ and $R_\sigma = 0.70$, were observed in cross sections where ΔK ranged between 20 and 35 $\text{MPa}\sqrt{m}$ and 14 and 17 $\text{MPa}\sqrt{m}$ respectively. To increase the experimental data population, cracks were measured on both the CT samples' surfaces. **Fig. 10** shows some remarkable examples of secondary cracks for the two orientations tested at different stress ratios. As can be seen, secondary cracks fraction and length are higher in Z-oriented samples at stress ratio $R_\sigma = 0.05$, also showing a more articulated path across the grains (**Fig. 10.a**). On the other hand, in the XY samples, large portions of the surface do not show any secondary cracks and the few of them which were analysed appear more linear with just a few ramifications (**Fig. 10.b**). This behaviour is even more evident for the samples tested at the higher stress ratio $R_\sigma = 0.70$, which is reported in **Fig. 10.c** and **Fig. 10.d** for the Z-oriented and XY-oriented specimens respectively.

This difference was further demonstrated by assessing the length of the visible secondary cracks in the Z and XY oriented CT specimens. The inspected portion of the material tested at $R_\sigma = 0.05$ was divided into three sub-regions, depending on the ΔK reached, more specifically 20-24, 25-29 and 30-35 $\text{MPa}\sqrt{m}$ respectively. **Fig. 11** shows the average secondary cracks length measured in the sub-regions previously mentioned. Secondary cracks were measured individually and, depending on their position, their length was associated with a specific column of the chart. The chart clearly evidences how secondary cracks are more likely to form in a Z-oriented sample than in an XY one. Moreover, the crack path in the Z-oriented samples is both intra and intergranular as shown in **Fig. 10.a-c**. The nucleation and growth of the secondary cracks, together with their continuous change in direction, may decrease the crack propagation energy which in turn, can be related to the lower propagation rate observed. On the other hand, XY samples have a more homogeneous microstructure and present fewer points for secondary cracks nucleation. This deeply impacts the crack growth behaviour, hindering the formation and propagation of secondary cracks. So, all the energy at disposal is dissipated through the propagation of the main crack which may travel faster until the final failure. This behaviour can be directly attributed to the anisotropy of the material (different properties) and its lower ductility in XY samples.

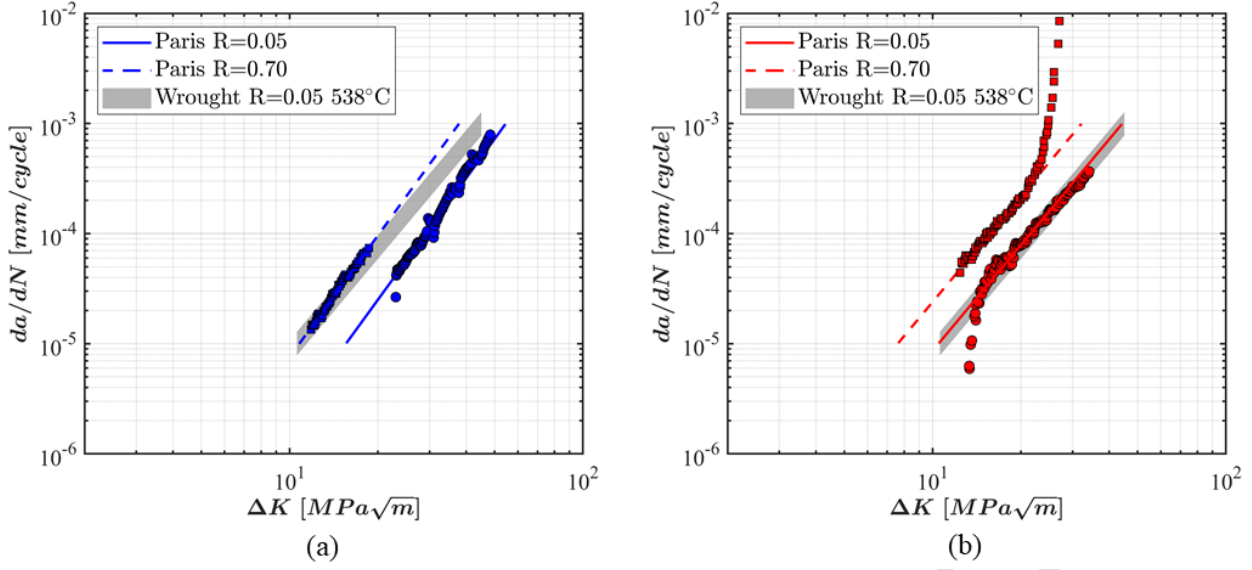


Figure 9: Paris' curve fitting for the fatigue crack growth results: a) fitting of the parameters for the Z printing direction; b) fitting of the parameters for the XY printing direction. The grey band represents the crack propagation results for wrought material tested at a temperature $T = 538\text{ }^{\circ}\text{C}$ and stress ratio $R_{\sigma} = 0.05$ from the work of James [49]. ΔK is in $[\text{MPa}\sqrt{\text{m}}]$ and da/dN is in $[\text{mm}/\text{cycle}]$.

Printing directions	m	$C_{0.05}$	$R^2_{0.05}$	$C_{0.70}$	$R^2_{0.70}$
Z	3.67	4.23E-10	0.77	1.62E-09	0.94
XY	3.19	5.60E-09	0.98	1.55E-08	0.98

Table 8: Parameters of Paris' law for the two printing directions fitted on the experimental data with the correlation coefficients. ΔK is in $[\text{MPa}\sqrt{\text{m}}]$ and da/dN is in $[\text{mm}/\text{cycle}]$.

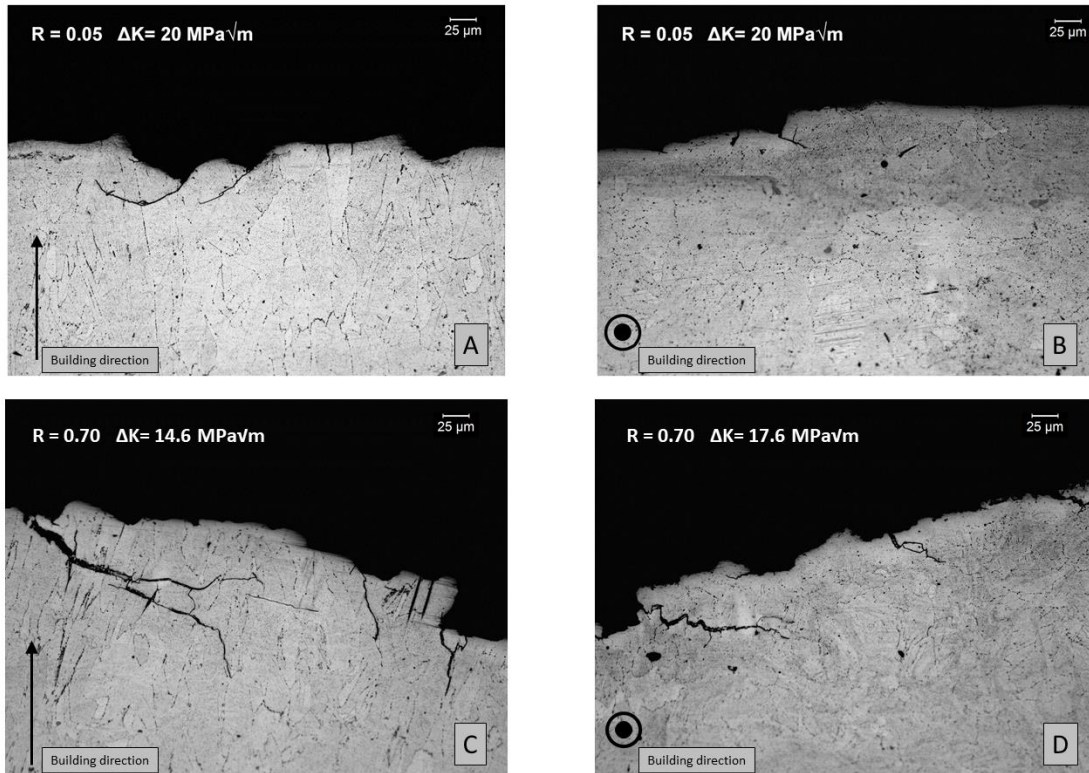


Figure 10: Secondary cracks in CT samples observed in cross sections for the building directions: a) Z direction with $\Delta K = 20 \text{ MPa}\sqrt{m}$; b) XY direction with $\Delta K = 20 \text{ MPa}\sqrt{m}$; c) Z direction with $\Delta K = 14.6 \text{ MPa}\sqrt{m}$; d) XY direction with $\Delta K = 17.6 \text{ MPa}\sqrt{m}$.

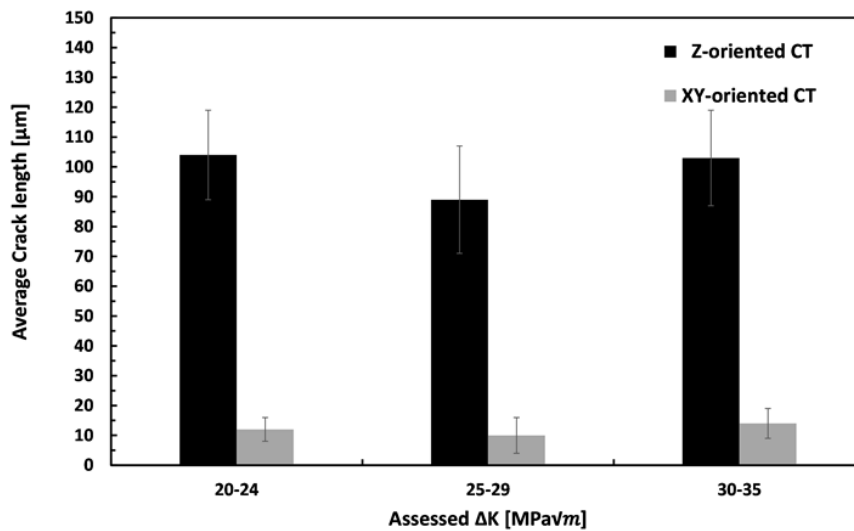


Figure 11: Secondary crack length as a function of sample orientation tested at stress ratio $R_\sigma = 0.05$.

4. Model for life prediction

The experimental findings demonstrated that the fatigue life of Inconel718 produced by AM is mainly affected by two aspects:

- The anisotropic mechanical behaviour due to different microstructures obtained for the two printing directions analysed.
- The presence of manufacturing defects, the dimensions of which vary from one series to the other.

To describe the fatigue life of a material with a certain intrinsic defectology, a fracture mechanics approach can be used. The material considered in this work undergoes alternate strain levels that are above the elastic limit, meaning that an approach based on linear elastic fracture mechanics (LEFM) would give non conservative estimations of the fatigue lives. For this reason an approach based on elasto-plastic fracture mechanics (EPFM) was adopted [50]. The crack driving force was then described with the adoption of an effective cyclic J-integral, which showed a good correlation with the experimental findings for different materials [33], [51]–[55]. The fatigue life in a high alternate strain regime can be then calculated by integrating the equation:

$$\frac{da}{dN} = C_J \cdot (\Delta J_{eff})^{m_J} \quad (7)$$

where C_J and m_J are material parameters fitted from crack propagation tests in an LCF regime. The cyclic J-integral was calculated with the generic formulation proposed by Rabbolini et al.[56]:

$$\Delta J_{eff} = Y^2 \cdot a \cdot PJ_{eff} \quad (8)$$

where Y is the crack shape factor and a is the crack length. The parameter PJ_{eff} has the following expression:

$$PJ_{eff} = \pi \cdot \left(\frac{\Delta \sigma_{eff}}{E'} + \frac{3}{4\sqrt{n'}} \cdot \Delta \sigma_{eff} \cdot \Delta \varepsilon_{pl,eff} \right) \quad (9)$$

where $E' = E/(1 - \nu^2)$ is the Young's modulus supposing a plane stress ahead of the internal crack tip and n' is the hardening exponent of the cyclic stress-strain curve. The effective stress range $\Delta \sigma_{eff}$ and the plastic strain range $\Delta \varepsilon_{pl,eff}$ were calculated from the stabilized hysteresis cycles once the crack opening and closure points had been identified:

$$\Delta \sigma_{eff} = \sigma_{max} - \sigma_{cl} \quad (10)$$

$$\Delta\varepsilon_{pl,eff} = \varepsilon_{max} - \varepsilon_{op} - \frac{\Delta\sigma_{eff}}{E'} \quad (11)$$

The stress at which the crack is found to be opened σ_{op} was estimated with the simplified model proposed by Newman [57], [58], where the constraint factor was taken to be $\alpha = 1$ supposing a large plastic zone while the flow stress was computed as:

$$\sigma_{flow} = \frac{R_{p,0.2} + R_m}{2} \quad (12)$$

The crack opening and closure was taken as happening at the same strain, in accordance with the work of Vormwald et al [59]. Once the opening stress had been computed, the corresponding strain was found from the loading branch of the stabilized hysteresis loop by means of a linear interpolation. The closure stress was then computed from the unloading branch of the stabilized hysteresis loop corresponding to the opening strain value.

The parameters of the crack growth law can be estimated from the long crack propagation tests reported in **Section 3.4**, by considering the relation between the elastic part of the cyclic J-integral and the stress intensity factor (SIF) range:

$$\Delta J_{el} = \frac{\Delta K^2}{E'} \quad (13)$$

Supposing that the long crack propagation tests at stress ratio $R_\sigma = 0.70$ were closure-free, and hence corresponding to the effective SIF range ΔK_{eff} , the parameters of **Equation 7** can be computed as:

$$m_J = \frac{m}{2} \quad (14)$$

$$C_J = C_{0.7} \cdot E'^{m_J} \quad (15)$$

To check the consistency of this hypothesis, the crack velocities computed using striation analysis in **Section 3.2** were plotted against the corresponding values estimated using **Equation 7**, where the ΔJ_{eff} parameter was computed from the stabilized hysteresis loop. In this graph the crack length for each data point was computed supposing a semi-circular crack with its centre at the initial defect position, passing through the point of the fracture surface analysed with the FE-SEM as shown in **Figure 6a** and **7a**. The results are plotted in **Fig. 12.a** for the Z series and in **Fig. 12.b** for the XY one.

Despite the uncertainty related to the manual procedure used to estimate crack speed from striations, the results are consistent with those obtained from the long crack tests.

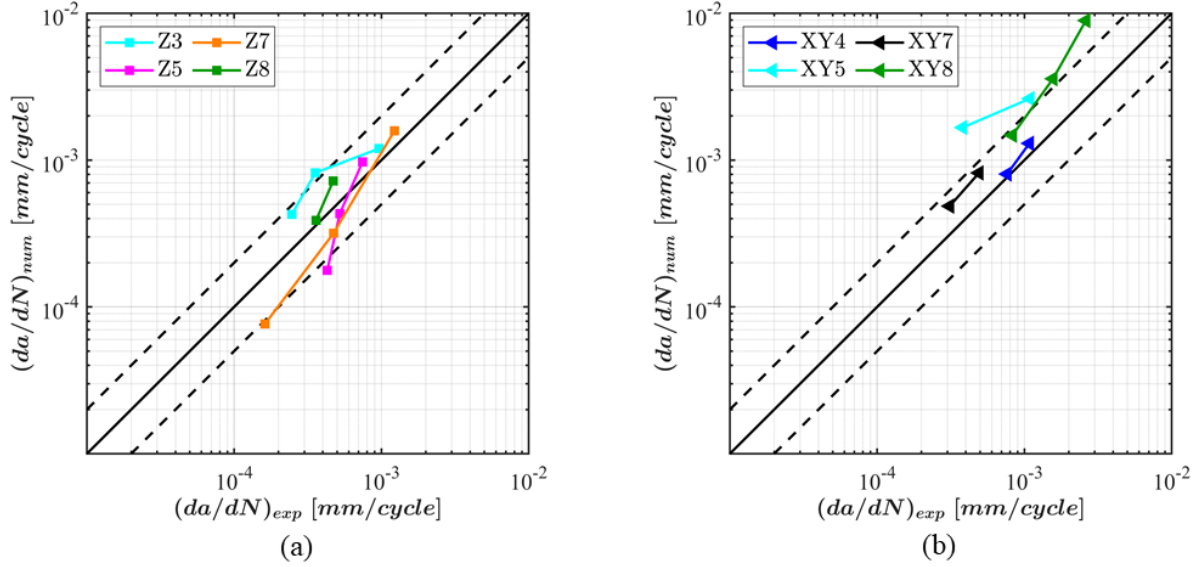


Figure 12: Comparison between the crack growth tests for long cracks in terms of ΔJ_{eff} and the crack speed estimated from striations of the LCF specimens: a) comparison for the Z direction data points; b) comparison for the XY direction data points.

It is reasonable to think that the printing direction with the higher defect size on average, is also the one with the lower fatigue life as reported in [21], [22]. Apparently, the comparison of life for series XY and Z specimens looks to contradict this solid fracture mechanics interpretation.

However, if we take into consideration the cyclic curves of the two printing directions reported in Fig. 5.a, it is evident that at the same applied alternate strain the resulting stress is higher for XY than for Z material. This results in a higher crack driving force for the specimens printed in the XY direction.

This is clearly shown in terms of PJ_{eff} in Fig. 13 where the two specimens tested at $\varepsilon_a = 0.55\%$ are compared. Specimen Z2 with a large defect had a lower PJ_{eff} than specimen XY8 (that had a defect four times smaller in terms of square root of area) because of the lower cyclic response.

Moreover, the anisotropy of the material also influences the crack propagation mechanism, as shown in Section 3.4. All these features lead to a lower fatigue life for specimen XY8 compared to Z2 (life of 4325 and 6225 cycles respectively).

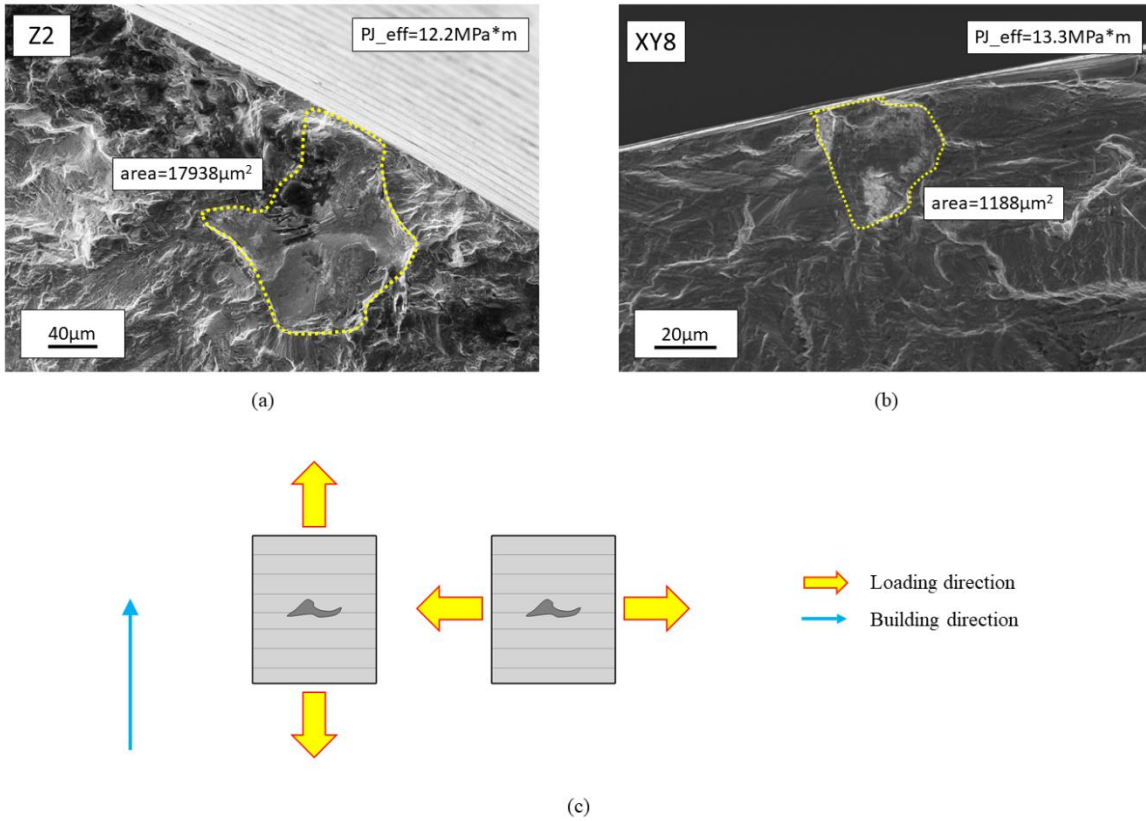


Figure 13: Dimension of killer defects responsible for the final rupture of specimens belonging to the two printing directions Z2 and XY8: a) SEM images of the defects found in a Z-oriented specimen; b) SEM images of the defects found in an XY-oriented specimen; c) scheme of the possible orientations of LoFs in relation to the loading and building orientations.

4.1 Verification of the crack growth model

In this section, the fatigue life of the tested samples is estimated using the fracture mechanics approach in LCF conditions, considering the defects found. The cracks were both taken as featuring a semicircular shape; this was supposed to remain constant during crack propagation, with an aspect ratio $a/c = 1$. The number of cycles to failure can then be computed using a numerical integration of **Equation 7**, once the parameter PJ_{eff} has been evaluated for each specimen. The integration of **Equation 7** requires the definition of the initial and final crack lengths a_i and a_f respectively. The initial crack length can be computed from the square root of area of the defects found \sqrt{area} collected in **Table 4**, assuming a semi-circular initial shape **Equation 16** gives:

$$a_i = \sqrt{area} \cdot \sqrt{2/\pi} \quad (16)$$

The final crack length was estimated from SEM observations of the fracture surfaces, that on average is equal to half the diameter of the specimen.

As previously discussed, the effective stress and plastic strain ranges were estimated from the experimentally stabilized hysteresis by employing the closure model proposed by Newman. The yielding stress $R_{p,0.2}$ in **Equation 12**, was estimated for the two printing directions from the initial loading ramps for the LCF specimens. From the initial loading ramp the monotonic Young's modulus was also estimated. Tensile tests on the material investigated material at 1000 °F were not performed, hence no data about the ultimate tensile stress was available. From the analysis of several works available in open literature [1], [60]–[63] a characteristic value of the ratio between ultimate tensile and yielding stress for Inconel718 produced using AM and tested at room temperature is about $R_m/R_{p,0.2} = 1.2$. Taking this observation into account the ultimate tensile stress R_m for the material analysed in this work can be easily estimated from the yielding stress for the two printing directions, the values obtained are collected in **Table 9**.

The shape factor Y considered in the crack growth simulations, varies for embedded and superficial cracks. For simplicity the shape factor Y was taken to be $Y_{surf} = 0.72$ and $Y_{int} = 0.64$ for superficial and embedded cracks [64] respectively. If an initial defect was categorized as embedded, Y_{int} was used for the initial propagation until the crack reaches the free surface. Once the crack reached the surface, it was considered to behave as a superficial crack and the Y_{surf} shape factor was used until the final rupture.

The estimated lives of the specimens tested are compared with the experimental results in **Fig. 14**, where the dashed black curves are scatter bands with a factor of 2 which is a common result in FCG simulations [65]. The numerical calculations correlate well with the experimental findings with a slight underestimation on the numerical side that is in favour of conservatism, with all the points contained within the scatter bands.

Printing direction	E [MPa]	$R_{p,0.2}$ [MPa]	R_m [MPa]
Z	137418	1163	1396
XY	158453	1214	1457

Table 9: Static properties of Inconel718 produced by SLM at 1000 °F: yielding stress estimated from LCF tests, ultimate tensile stress estimated as 20% higher than the yielding stress.

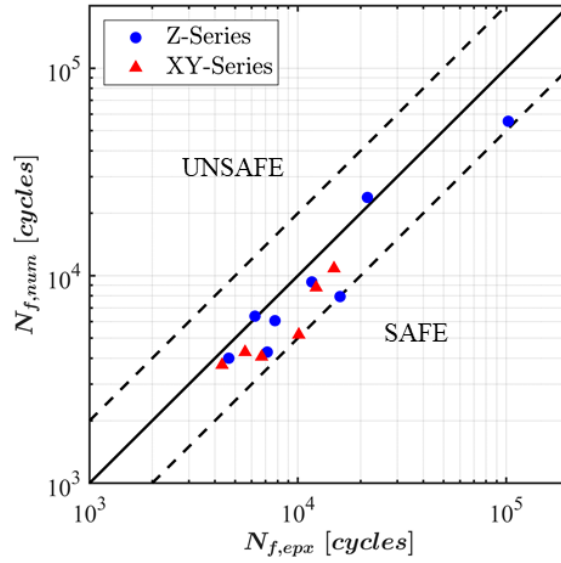


Figure 14: Comparison between the experimental results of LCF tests versus the numerical estimations using the fracture mechanics model.

4.2 Life prediction

To estimate the fatigue life of a component made of Inconel718 obtained using AM, one has to take into account the anisotropic mechanical behaviour of the parts which are printed with different orientations in relation to the building plan. Once finite element modelling (FEM) of the component is finished, the fatigue life can be estimated using the elasto-plastic crack propagation model by choosing the material parameters related to the printing orientation of the zone considered. The numerical integration of the crack propagation model described by **Equation 7** in case of very complex components could be a non trivial task; for this reason in this **Section** a simplified fatigue model which takes into account both the anisotropy of the material and the presence of manufacturing defects is proposed.

The proposed model is basically an extension of the Coffin-Manson curves in the presence of defects. The cyclic mechanical behaviour of material was described using the Ramberg-Osgood curves obtained with the two different printing directions (see **Section 3.1**), disregarding cyclic hardening or softening. From the experimental evidence the hypothesis of having a stable cyclic mechanical response, was found to be a good approximation for the alternate strain ranges considered in this work. The cyclic curve is different from the tensile one; if the Ramberg-Osgood curve was used to estimate the first loading ramp as well, the fatigue calculations lead to overconservative estimations. To overcome this problem, the first loading ramp was described, for both the printing directions, using the elasto-plastic curve fitted on the experimental loading ramp. The hysteresis cycles were then numerically estimated, which is the input for the numerical integration of **Equation**

7. Two different percentiles of the statistical defects distribution presented in **Section 3.3** were considered, namely 50% and 97.5%, to obtain the initial crack size a_i according to **Equation 16**. The integration was stopped when the final crack size a_f was reached, which is taken as corresponding to half the diameter of the LCF specimens, i.e. 3 mm. The crack shape factor was taken to be constant, supposing that each crack starts propagating from the specimen's free surface.

Fig. 15 shows the results of the numerical endurance curves obtained compared with the experimental results of the LCF tests, the solid lines refer to the 50% percentile while the dashed ones to the 97.5% percentile of the statistical distribution of defects. As can be seen, the numerical curve for the Z-oriented specimens fits well with the experimental findings with a slight underestimation. The numerical estimations of fatigue lives for the XY series are also satisfactory, showing a systematic underestimation compared to the experimental results. The crack propagation model adopted in this work, only takes into account the stable propagation regime, disregarding the near threshold and the nucleation time from defects. Due to the very small size of the killer defects of the XY series it can be expected that the simplifications may lead to conservative life prediction. The mean dimension of the found defects from XY tested material resulted to be near those of the material grains, leading to an interaction with the microstructure [44] and hence a crack retardation. With these numerical curves a designer can simply calculate the fatigue life of a component, using simply the amplitude of the cyclic strain as an input.

The proposed methodology was validated considering smooth specimens, hence only the effect of internal defects was taken into account, disregarding the effects of the "As-Built" rough surface. In literature there are several works dealing with the high cycle fatigue of AM material considering the effect of the rough surface left by the manufacturing process [22], [66], [75], [67]–[74] and modelling it in terms of propagation of the surface features. It is then expected that the present approach could allow application of the same concepts to LCF conditions, even if the surface features are usually modelled as 2-D cracks, and not as semi-circular defects.

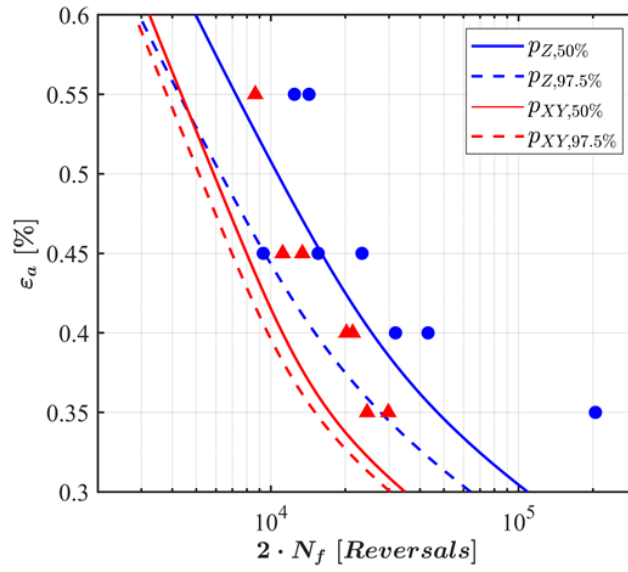


Figure 15: Numerical estimation of the Coffin-Manson curves using a fracture mechanics approach for the two building orientations and the two percentiles of the distribution of defects. The experimental points are blue circles for Z specimens and red triangles for XY specimens.

Accepted Manuscript

5. Conclusions

In this study the influence of macroscopic anisotropy and the presence of manufacturing defects were investigated on the fatigue life in LCF conditions for the Ni-based superalloy Inconel718 obtained using AM and tested at 1000 °F temperature. The fatigue life was estimated using a fracture mechanics approach to take into account the presence of manufacturing defects. The main conclusions are listed below:

- The printing direction of the material influences its microstructure, leading to an anisotropic mechanical behaviour. The texture obtained cannot be modified with the standard heat treatments.
- The material's anisotropy influences not only the mechanical behaviour under operating conditions, but also crack propagation. It was found that in Z-oriented specimens the main crack features vertical ramifications that slow down the propagation leading to higher fatigue strength compared to the XY orientation, which was found to be about 45% lower than the Z oriented ones at the highest strain range.
- The mean defect size for the XY oriented specimens was found to be three times lower than their Z oriented counterparts. This is in line with other works published in literature. Nonetheless, the fatigue life of the Z oriented specimens was found to be higher due to both the anisotropic mechanical behaviour and the different crack growth rate.
- The proposed methodology can be adopted to easily assess the fatigue life of a component produced using AM and subjected to an elasto-plastic state of stress. Despite the simplifications adopted, the numerical estimations based on the stabilized cyclic behaviour and ΔJ_{eff} approach show satisfactory results.

Acknowledgments

Contributions made to this paper include: (i) F. Sausto performed part of the tests together with modelling and analyses, and he took care of preparing the manuscript; (ii) G. Marchese and E. Bassini took care of the microstructural analyses of the samples. (iii) S. Biamino and D. Ugues took care of the calibration of the manufacturing process and the building of the samples tested. (iv) S. Foletti helped with the elasto-plastic crack propagation model and the schematization of the paper. (v) S. Beretta directed this research on defect-based analysis and contributed to the manuscript. The authors would like to acknowledge the Integrated Additive Manufacturing Centre at Politecnico di Torino (IAM@PoliTo) where the specimens were fabricated and characterized.

Accepted Manuscript

References

- [1] E. Chlebus, K. Gruber, B. Kuźnicka, J. Kurzac, and T. Kurzynowski, Effect of heat treatment on the microstructure and mechanical properties of Inconel 718 processed by selective laser melting, *Mater. Sci. Eng. A*, vol. 639, pp. 647–655, 2015, doi: 10.1016/j.msea.2015.05.035.
- [2] M. M. Attallah, R. Jennings, X. Wang, and L. N. Carter, Additive manufacturing of Ni-based superalloys: The outstanding issues, *MRS Bull.*, vol. 41, no. 10, pp. 758–764, Oct. 2016, doi: 10.1557/mrs.2016.211.
- [3] S. Soller *et al.*, Selective laser melting (SLM) of Inconel 718 and stainless steel injectors for liquid rocket engines, *Sp. Propuls. 2016 Proc.*, 2016.
- [4] S. Soller *et al.*, Design and testing of liquid propellant injectors for additive manufacturing, 2017.
- [5] D. Herzog, V. Seyda, E. Wycisk, and C. Emmelmann, Additive manufacturing of metals, *Acta Mater.*, vol. 117, pp. 371–392, 2016.
- [6] E. O. Ezugwu, Key improvements in the machining of difficult-to-cut aerospace superalloys, *Int. J. Mach. Tools Manuf.*, vol. 45, no. 12–13, pp. 1353–1367, 2005.
- [7] D. Deng, R. L. Peng, H. Brodin, and J. Moverare, Microstructure and mechanical properties of Inconel 718 produced by selective laser melting: Sample orientation dependence and effects of post heat treatments, *Mater. Sci. Eng. A*, vol. 713, pp. 294–306, 2018.
- [8] V. A. Popovich, E. V Borisov, A. A. Popovich, V. S. Sufiiarov, D. V Masaylo, and L. Alzina, Functionally graded Inconel 718 processed by additive manufacturing: Crystallographic texture, anisotropy of microstructure and mechanical properties, *Mater. Des.*, vol. 114, pp. 441–449, 2017.
- [9] X. Gong, X. Wang, V. Cole, Z. Jones, K. Cooper, and K. Chou, Characterization of microstructure and mechanical property of Inconel 718 from selective laser melting, 2015.
- [10] Y. Tian *et al.*, Rationalization of microstructure heterogeneity in INCONEL 718 builds made by the direct laser additive manufacturing process, *Metall. Mater. Trans. A*, vol. 45, no. 10, pp. 4470–4483, 2014.
- [11] L. C. Ardila *et al.*, Effect of IN718 recycled powder reuse on properties of parts manufactured by means of Selective Laser Melting, *Phys. Procedia*, vol. 56, pp. 99–107, 2014.

- [12] M. Calandri *et al.*, Solution treatment study of Inconel 718 produced by SLM additive technique in view of the oxidation resistance, *Adv. Eng. Mater.*, vol. 20, no. 11, p. 1800351, 2018.
- [13] M. Calandri, S. Yin, B. Aldwell, F. Calignano, R. Lupoi, and D. Ugues, Texture and Microstructural Features at Different Length Scales in Inconel 718 Produced by Selective Laser Melting., *Mater. (Basel, Switzerland)*, vol. 12, no. 8, 2019.
- [14] D. Zhang, Z. Feng, C. Wang, W. Wang, Z. Liu, and W. Niu, Comparison of microstructures and mechanical properties of Inconel 718 alloy processed by selective laser melting and casting, *Mater. Sci. Eng. A*, vol. 724, pp. 357–367, 2018.
- [15] X. Wang and K. Chou, Effects of thermal cycles on the microstructure evolution of Inconel 718 during selective laser melting process, *Addit. Manuf.*, vol. 18, pp. 1–14, 2017.
- [16] G. H. Cao *et al.*, Investigations of γ' , γ'' and $\delta\delta$ precipitates in heat-treated Inconel 718 alloy fabricated by selective laser melting, *Mater. Charact.*, vol. 136, pp. 398–406, 2018.
- [17] L. N. Carter *et al.*, Process optimisation of selective laser melting using energy density model for nickel based superalloys, *Mater. Sci. Technol.*, vol. 32, no. 7, pp. 657–661, 2016.
- [18] G. Marchese *et al.*, Microstructural investigation of as-fabricated and heat-treated Inconel 625 and Inconel 718 fabricated by direct metal laser sintering: Contribution of Politecnico di Torino and Istituto Italiano di Tecnologia (IIT) di Torino, *Met. Powder Rep.*, vol. 71, no. 4, pp. 273–278, 2016.
- [19] D. Zhang, W. Niu, X. Cao, and Z. Liu, Effect of standard heat treatment on the microstructure and mechanical properties of selective laser melting manufactured Inconel 718 superalloy, *Mater. Sci. Eng. A*, vol. 644, pp. 32–40, 2015, doi: 10.1016/j.msea.2015.06.021.
- [20] M. Ni *et al.*, Anisotropic tensile behavior of in situ precipitation strengthened Inconel 718 fabricated by additive manufacturing, *Mater. Sci. Eng. A*, vol. 701, pp. 344–351, 2017.
- [21] A. Yadollahi, N. Shamsaei, S. M. Thompson, A. Elwany, and L. Bian, Effects of building orientation and heat treatment on fatigue behavior of selective laser melted 17-4 PH stainless steel, *Int. J. Fatigue*, vol. 94, pp. 218–235, 2017.
- [22] R. Shrestha, J. Simsiriwong, and N. Shamsaei, Fatigue behavior of additive manufactured 316L stainless steel parts: Effects of layer orientation and surface roughness, *Addit. Manuf.*,

vol. 28, pp. 23–38, 2019.

- [23] A. Riemer, S. Leuders, M. Thöne, H. A. Richard, T. Tröster, and T. Niendorf, On the fatigue crack growth behavior in 316L stainless steel manufactured by selective laser melting, *Eng. Fract. Mech.*, vol. 120, pp. 15–25, 2014, doi: 10.1016/j.engfracmech.2014.03.008.
- [24] T. Lindström, M. Calmunger, R. Eriksson, and D. Leidermark, Fatigue behaviour of an additively manufactured ductile gas turbine superalloy, *Theor. Appl. Fract. Mech.*, p. 102604, 2020.
- [25] A. R. Balachandramurthi, J. Moverare, N. Dixit, and R. Pederson, Influence of defects and as-built surface roughness on fatigue properties of additively manufactured Alloy 718, *Mater. Sci. Eng. A*, vol. 735, no. August, pp. 463–474, 2018, doi: 10.1016/j.msea.2018.08.072.
- [26] A. S. Johnson, S. Shao, N. Shamsaei, S. M. Thompson, and L. Bian, Microstructure, Fatigue Behavior, and Failure Mechanisms of Direct Laser-Deposited Inconel 718, *Jom*, vol. 69, no. 3, pp. 597–603, 2017, doi: 10.1007/s11837-016-2225-2.
- [27] D. B. Witkin, D. Patel, T. V. Albright, G. E. Bean, and T. McLouth, Influence of surface conditions and specimen orientation on high cycle fatigue properties of Inconel 718 prepared by laser powder bed fusion, *Int. J. Fatigue*, vol. 132, no. November 2019, p. 105392, 2020, doi: 10.1016/j.ijfatigue.2019.105392.
- [28] Z. Zhou, X. Hua, C. Li, and G. Chen, The effect of texture on the low cycle fatigue property of Inconel 718 by selective laser melting, *MATEC Web Conf.*, vol. 165, pp. 0–3, 2018, doi: 10.1051/mateconf/201816502007.
- [29] A. R. Balachandramurthi, J. Moverare, T. Hansson, and R. Pederson, Anisotropic fatigue properties of Alloy 718 manufactured by Electron Beam Powder Bed Fusion, *Int. J. Fatigue*, vol. 141, no. August, p. 105898, 2020, doi: 10.1016/j.ijfatigue.2020.105898.
- [30] A. Ramanathan Balachandramurthi, J. Moverare, T. Hansson, and R. Pederson, *Anisotropic fatigue properties of Alloy 718 manufactured by Electron Beam Powder Bed Fusion*. Elsevier Ltd, 2020.
- [31] M. M. Kirka, D. A. Greeley, C. Hawkins, and R. R. Dehoff, Effect of anisotropy and texture on the low cycle fatigue behavior of Inconel 718 processed via electron beam melting, *Int. J. Fatigue*, vol. 105, pp. 235–243, 2017, doi: 10.1016/j.ijfatigue.2017.08.021.

- [32] P. D. Nezhadfar, A. S. Johnson, and N. Shamsaei, Fatigue Behavior and Microstructural Evolution of Additively Manufactured Inconel 718 under Cyclic Loading at Elevated Temperature, *Int. J. Fatigue*, p. 105598, 2020.
- [33] S. Romano, L. Patriarca, S. Foletti, and S. Beretta, LCF behaviour and a comprehensive life prediction model for AlSi10Mg obtained by SLM, *Int. J. Fatigue*, vol. 117, pp. 47–62, 2018.
- [34] ASTM E606/E606M-12, Standard Test Method for Strain-Controlled Fatigue Testing, vol. 03.01. ASTM International, West Conshohocken, PA, 2012, doi: 10.1520/E0606-04E01.Copyright.
- [35] A. E647-00, Standard test method for measurement of fatigue crack growth rates, 2004.
- [36] M. Clavel and A. Pineau, Frequency and Wave-Form Effects on the Fatigue Crack Growth Behavior of Alloy 718 At 298 K and 823 K., *Met. Trans A*, vol. 9 A, no. 4, pp. 471–480, 1978, doi: 10.1007/BF02646402.
- [37] ASTM E399-19, Standard Test Method for Linear-Elastic Plane-Strain Fracture Toughness K_{Ic} of Metallic Materials. ASTM International, West Conshohocken, PA, 2019.
- [38] D. Fournier and A. Pineau, Low cycle fatigue behavior of Inconel 718 at 298 K and 823 K, *Metall. Trans. A*, vol. 8, no. 7, pp. 1095–1105, 1977.
- [39] C. R. Brinkman and G. E. Korth, Strain Fatigue and Tensile Behavior of Inconel®718 from Room Temperature to 650 C, *J. Test. Eval.*, vol. 2, no. 4, pp. 249–259, 1974.
- [40] S. Suresh, *Fatigue of materials 2nd edition*. Cambridge university press, 2006.
- [41] Y. Murakami, *Metal fatigue: effects of small defects and nonmetallic inclusions*. Academic Press, 2019.
- [42] C. C. Battaile, J. M. Emery, L. N. Brewer, and B. L. Boyce, Crystal plasticity simulations of microstructure-induced uncertainty in strain concentration near voids in brass, *Philos. Mag.*, vol. 95, no. 10, pp. 1069–1079, 2015, doi: 10.1080/14786435.2015.1009958.
- [43] R. Cunningham *et al.*, Analyzing the effects of powder and post-processing on porosity and properties of electron beam melted Ti-6Al-4V, *Mater. Res. Lett.*, vol. 5, no. 7, pp. 516–525, 2017.
- [44] V. Prithvirajan and M. D. Sangid, The role of defects and critical pore size analysis in the fatigue response of additively manufactured IN718 via crystal plasticity, *Mater. Des.*, vol. 150, pp. 139–153, 2018.

- [45] M. D. Sangid, P. Ravi, V. Prithivirajan, N. A. Miller, P. Kenesei, and J.-S. Park, ICME Approach to Determining Critical Pore Size of IN718 Produced by Selective Laser Melting, *JOM*, vol. 72, no. 1, pp. 465–474, 2020.
- [46] P. J. E. Forsyth and D. A. Ryder, Fatigue fracture, *Aircr. Eng. Aerosp. Technol.*, 1960.
- [47] G. Jacoby, Fractographic methods in fatigue research, *Exp. Mech.*, vol. 5, no. 3, pp. 65–82, 1965.
- [48] R. Koteraiawa, M. Mori, T. Matsui, and D. Shimo, Fractographic study of fatigue crack propagation, *J. Eng. Mater. Technol. Trans. ASME*, vol. 95, no. 4, pp. 202–212, 1973, doi: 10.1115/1.3443154.
- [49] L. A. James, Fatigue-crack propagation behavior of inconel 718, 1975.
- [50] N. E. Dowling, Cyclic stress-strain and plastic deformation aspects of fatigue crack growth, *ASTM STP*, vol. 637, no. 97, p. 121, 1977.
- [51] R. C. McClung and H. Sehitoglu, Closure behavior of small cracks under high strain fatigue histories, in *Mechanics of fatigue crack closure*, ASTM International, 1988.
- [52] M. Vormwald, the Consequences of Short Crack Closure on Fatigue Crack Growth Under Variable Amplitude Loading, *Fatigue Fract. Eng. Mater. Struct.*, vol. 14, no. 213, pp. 205–225, 1991, [Online]. Available: internal-pdf://66.82.96.200/1991_Vormwald_The consequences of short crac.pdf.
- [53] S. Rabbolini, S. Beretta, S. Foletti, and A. Riva, Short crack propagation in LCF regime at room and high temperature in Q & T rotor steels, *Int. J. Fatigue*, vol. 75, pp. 10–18, 2015, doi: 10.1016/j.ijfatigue.2015.01.009.
- [54] S. Rabbolini, S. Beretta, S. Foletti, and M. E. Cristea, Crack closure effects during low cycle fatigue propagation in line pipe steel: An analysis with digital image correlation, *Eng. Fract. Mech.*, 2015, doi: 10.1016/j.engfracmech.2015.07.070.
- [55] L. Patriarca, S. Foletti, and S. Beretta, A comparison of DIC-based techniques to measure crack closure in LCF, *Theor. Appl. Fract. Mech.*, Oct. 2018, doi: 10.1016/J.TAFMEC.2018.09.020.
- [56] S. Rabbolini, S. Beretta, S. Foletti, and M. E. Cristea, Crack closure effects during low cycle fatigue propagation in line pipe steel: An analysis with digital image correlation, *Eng. Fract. Mech.*, vol. 148, pp. 441–456, 2015, doi: 10.1016/j.engfracmech.2015.07.070.

- [57] J. C. J. Newman, A crack-closure model for predicting fatigue crack growth under aircraft spectrum loading, *Methods Model. Predict. Fatigue Crack Growth under Random Load.*, vol. 748, pp. 53–84, 1981, doi: 10.1520/STP28334S.
- [58] J. C. Newman Jr, A crack opening stress equation for fatigue crack growth, 1984.
- [59] M. Vormwald and T. Seeger, The Consequences of Short Crack Closure on Fatigue Crack Growth Under Variable Amplitude Loading, *Fatigue Fract. Eng. Mater. Struct.*, vol. 14, no. 2/3, pp. 205–225, 1991.
- [60] Q. Zhang, J. Yao, and J. Mazumder, Laser direct metal deposition technology and microstructure and composition segregation of Inconel 718 superalloy, *J. Iron Steel Res. Int.*, vol. 18, no. 4, pp. 73–78, 2011.
- [61] X. Zhao, J. Chen, X. Lin, and W. Huang, Study on microstructure and mechanical properties of laser rapid forming Inconel 718, *Mater. Sci. Eng. A*, vol. 478, no. 1–2, pp. 119–124, 2008.
- [62] K. N. Amato *et al.*, Microstructures and mechanical behavior of Inconel 718 fabricated by selective laser melting, *Acta Mater.*, vol. 60, no. 5, pp. 2229–2239, 2012.
- [63] P. L. Blackwell, The mechanical and microstructural characteristics of laser-deposited IN718, *J. Mater. Process. Technol.*, vol. 170, no. 1–2, pp. 240–246, 2005.
- [64] N. E. Dowling, Engineering methods for deformation, fracture and fatigue, *Mech. Behav. Mater. 4th ed. Pearson Prentice Hall*, pp. 360–365, 2013.
- [65] P. Heuler and W. Schuetz, Assessment of concepts for fatigue crack initiation and propagation life prediction, *Materwiss. Werksttech.*, vol. 17, no. 11, pp. 397–405, 1986.
- [66] D. Greitemeier, C. Dalle Donne, F. Syassen, J. Eufinger, and T. Melz, Effect of surface roughness on fatigue performance of additive manufactured Ti-6Al-4V, *Mater. Sci. Technol.*, vol. 32, no. 7, pp. 629–634, 2016, doi: 10.1179/1743284715Y.0000000053.
- [67] S. Beretta, M. Gargourimotlagh, S. Foletti, A. du Plessis, and M. Riccio, Fatigue strength assessment of “as built” AlSi10Mg manufactured by SLM with different build orientations, *Int. J. Fatigue*, vol. 139, 2020, doi: 10.1016/j.ijfatigue.2020.105737.
- [68] A. du Plessis and S. Beretta, Killer notches: The effect of as-built surface roughness on fatigue failure in AlSi10Mg produced by laser powder bed fusion, *Addit. Manuf.*, vol. 35, no. June, p. 101424, 2020, doi: 10.1016/j.addma.2020.101424.
- [69] H. Masuo *et al.*, Influence of defects, surface roughness and HIP on the fatigue strength of

Ti-6Al-4V manufactured by additive manufacturing, *Int. J. Fatigue*, vol. 117, no. July, pp. 163–179, 2018, doi: 10.1016/j.ijfatigue.2018.07.020.

- [70] C. Dalle Donne, F. Syassen, T. Melz, D. Greitemeier, and J. Eufinger, Effect of surface roughness on fatigue performance of additive manufactured Ti–6Al–4V, *Mater. Sci. Technol.*, 2015, doi: 10.1179/1743284715y.0000000053.
- [71] A. Yadollahi, M. J. Mahtabi, A. Khalili, H. R. Doude, and J. C. Newman, Fatigue life prediction of additively manufactured material: Effects of surface roughness, defect size, and shape, *Fatigue Fract. Eng. Mater. Struct.*, 2018, doi: 10.1111/ffe.12799.
- [72] R. Molaei and A. Fatemi, Crack paths in additive manufactured metallic materials subjected to multiaxial cyclic loads including surface roughness, HIP, and notch effects, *Int. J. Fatigue*, vol. 124, no. December 2018, pp. 558–570, 2019, doi: 10.1016/j.ijfatigue.2019.03.007.
- [73] H. Y. Wan *et al.*, Effects of surface roughness and build thickness on fatigue properties of selective laser melted Inconel 718 at 650 °C, *Int. J. Fatigue*, vol. 137, no. April, 2020, doi: 10.1016/j.ijfatigue.2020.105654.
- [74] J. Zhang and A. Fatemi, Surface roughness effect on multiaxial fatigue behavior of additive manufactured metals and its modeling, *Theor. Appl. Fract. Mech.*, vol. 103, no. December 2018, p. 102260, 2019, doi: 10.1016/j.tafmec.2019.102260.
- [75] T. Persenot, A. Burr, G. Martin, J. Y. Buffiere, R. Dendievel, and E. Maire, Effect of build orientation on the fatigue properties of as-built Electron Beam Melted Ti-6Al-4V alloy, *Int. J. Fatigue*, vol. 118, no. July 2018, pp. 65–76, 2019, doi: 10.1016/j.ijfatigue.2018.08.006.

Appendix

The following tables show the results of the LCF tests at 1000 °F for the two printing directions.

ID	σ_a [MPa]	ε_a [mm/mm]	$R_\varepsilon = \frac{\varepsilon_{min}}{\varepsilon_{max}}$	$R_\sigma = \frac{\sigma_{min}}{\sigma_{max}}$	E [MPa]	N_f [cycles]
Z1	640	0,0045	0	-0,17	147608	11671
Z2	713	0,0055	0	-0,51	133850	6225
Z3	624	0,0045	0	-0,16	143854	7765
Z4	748	0,0055	0	-0,36	138245	7130
Z5	487	0,0035	0	-0,08	147473	102315
Z6	619	0,0045	0	-0,14	141387	4660
Z7	583	0,004	0	-0,16	148414	21572
Z8	555	0,004	0	-0,14	142786	15940

Table 10: Results of the LCF tests at 1000 °F for the Z-series specimens considering a strain ratio of $R_\varepsilon = 0$.

ID	σ_a [MPa]	ε_a [mm/mm]	$R_\varepsilon = \frac{\varepsilon_{min}}{\varepsilon_{max}}$	$R_\sigma = \frac{\sigma_{min}}{\sigma_{max}}$	E [MPa]	N_f [cycles]
XY1	737	0,0045	0	-0,30	167988	5580
XY3	652	0,0040	0	-0,15	167988	10702
XY4	565	0,0035	0	-0,05	160569	12241
XY5	709	0,0045	0	-0,23	159692	6700
XY6	647	0,0040	0	-0,13	165342	10100
XY7	565	0,0035	0	-0,12	164592	14910
XY8	828	0,0055	0	-0,55	154134	4325

Table 11: Results of the LCF tests at 1000 °F for the XY-series specimens considering a strain ratio of $R_\varepsilon = 0$.